Catalysis Science & Technology

Atomic-scale Secondary Electron Imaging for Heterogeneous Catalysis Research

Journal:	*Catalysis Science & Technology*
Manuscript ID	CY-REV-12-2024-001551.R1
Article Type:	Review Article
Date Submitted by the Author:	28-Feb-2025
Complete List of Authors:	Hwang, Sooyeon; Brookhaven National Laboratory, Center for Functional Nanomaterials Yang, Judith; University of Pittsburgh, Department of Chemical and Petroleum Engineering; Brookhaven National Laboratory; University of Pittsburgh, Department of Physics

Atomic-scale Secondary Electron Imaging for Heterogeneous Catalysis Research

Sooyeon Hwang*, Judith C. Yang

Center for Functional Nanomaterials, Brookhaven National Laboratory, Upton, New York 11973

Characterizing the surface at the atomic scale is essential for understanding the catalytic properties of supported metal nanoparticles. Secondary electron (SE) imaging in scanning transmission electron microscopy (STEM) provides three-dimensional surface topographic information, enabling the characterization of the size, morphology, and distribution of supported nanoparticles. Furthermore, real-time observation of catalyst materials in a gaseous environment enhances our understanding of catalyst dynamics under operational conditions. Ongoing technical developments in SE-STEM, along with advancements in computational methods, are expected to facilitate atomic-scale surface observations and enable more quantitative and statistical analyses. This progress will not only elucidate fundamental mechanisms at the atomic level but also provide comprehensive and universal insights into catalyst performance. This minireview showcases the recent advancements and research findings in surface-sensitive SE imaging in STEM for the characterization of active catalyst materials.

*Corresponding author: soohwang@bnl.gov

Introduction

Catalysis plays a key role in academic research and industry, with widespread applications in everyday life. Nearly all chemical products are synthesized through at least one catalytic step, highlighting its significant impact on modern society.[1, 2] Moreover, catalysis holds great promise for advancing sustainable energy solutions by contributing to energy production, storage, transportation, and enhancing energy efficiency.[3-5] Heterogeneous catalysts, which are in different phases from the reaction mixture, dominate the various applications including polymer industry; coal, oil and gas refining; manufacturing chemicals; environmental applications; and electrochemical energy conversion and storage devices.[6-8] Most heterogeneous catalysts are supported metal nanomaterials, where active metals are finely distributed on a support with a high surface area. The active metal component generally has specific active sites on its surface where catalytic reaction occurs. Therefore, reducing the size of active metal to nanoscale or even to atomic clusters have proven to be an effective strategy to maximize the number of active sites and boost performance of catalyst.[9-12]

To enhance catalyst performance through particle downsizing and surface engineering, the utilization of advanced characterization tools is essential for verifying structural features. Electron microscopy has successfully served to image catalysts at small scales. Scanning electron microscopy (SEM) has been extensively used for decades as a primary technique for examining morphology of catalysts.[13-17] Transmission electron microscopy (TEM) and scanning transmission electron microscopy (STEM), have provided valuable insights into not only about particle size and shape but also the lattice structures.[18-22] The development of aberration correctors has further enhanced the spatial resolution of S/TEM, making atomic-resolution imaging routine.[23-26] Despite their widespread use, neither SEM nor S/TEM offers a complete solution for characterizing catalyst structures. While SEM provides three-dimensional (3D) structure information via surface topography, the primary limitation lies in its spatial resolution, typically constrained to the nanometer scale. In contrast, S/TEM offers sub-angstrom spatial resolution with aberration-correction. However, the resulting images are two-dimensional projections, indicating that S/TEM captures only a partial view of the 3D structure of the catalyst/support system. In addition, the minimal surface sensitivity of S/TEM suggests that critical surface features relevant to catalysis may not be captured, potentially limiting its applicability in accessing the catalyst's performance.

Electron tomography using S/TEM has enabled the reconstruction of 3D structures in materials at high resolution, but the acquisition of tilt series and following image reconstruction typically requires more than hours, which poses a challenge for capturing time-resolved information.[27, 28] Considering the similar electron probe scanning mechanism in both SEM and STEM, introducing surface sensitivity into STEM could be ideal for investigating surface topography as well as the overall material at atomic resolution without sacrificing time resolution. This minireview will briefly introduce the concept of integrating SEM imaging with advanced STEM, highlighting examples of this technique applied to catalyst studies. The goal is to offer researchers in the catalysis field valuable insights into the cutting-edge electron microscopy methods, inspiring their application to future catalysis studies.

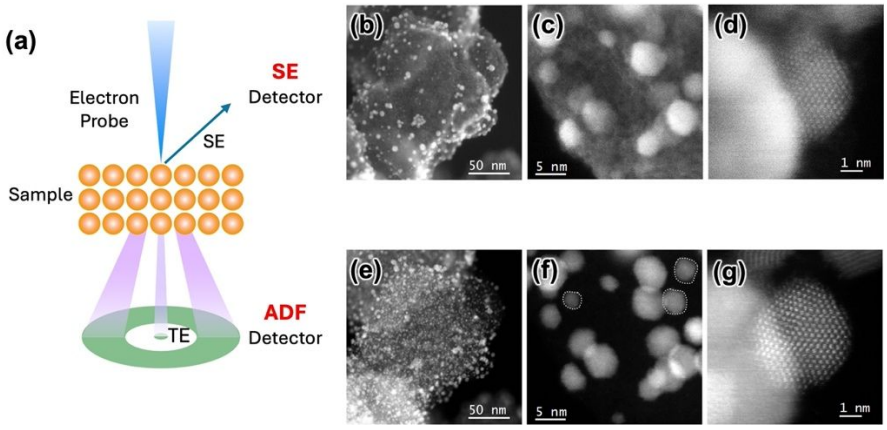

Figure 1. (a) Schematic representation of secondary electron (SE) and annular dark field (ADF) imaging techniques. Platinum nanoparticles on a carbon support are shown in (b-d) as SE images, and in (e-g) as high-angle annular dark field scanning transmission electron microscopy (HAADF-STEM) images of the same region at different magnifications. The particles marked in (f) are absent in (c), indicating that they are likely subsurface and not exposed on the surface.

SE imaging in STEM

When an electron beam interacts with a specimen, a variety of signals are emitted from the specimen, including secondary electrons (SE).[29] SEs are generated through the inelastic scattering, typically with energies less than 50 eV. Only SEs near the surface can escape, make them detectable. The escape depth of the SEs from metals is about 0.5-1.5 nm, while for insulators, it ranges from 10 to 20 nm.[30] Due to the limited escape depth of SEs, they are highly surface-sensitive and they serve as the primary source for SEM imaging to display surface topography.[31]

SE imaging has been successfully demonstrated by incorporating a SE detector within the STEM,[32] providing topographic information of supported particles and particle data for catalysis with sub-nanometer spatial resolution.[33-35] A pioneering achievement was reported by Zhu *et al*., showcased atomic resolution SE imaging enabled by aberration-corrected electron probe.[36] They positioned the SE detector above the sample, while an annular dark field detector (ADF) for general STEM imaging was placed below the sample to capture electrons transmitted through it (Figure 1a), enabling simultaneous SE and ADF-STEM imaging. Theoretical and experimental demonstration of atomic resolution SE imaging have been conducted,[37-42] and the field of catalysis has benefitted from this imaging technique in the following ways.

SE imaging in STEM for Catalysts

Figure 1(b-d) and (e-g) present SE images and high-angle annular dark-field STEM (HAADF-STEM) images, respectively, acquired from the same areas of Pt/C catalysts at various magnifications using aberration-corrected STEM with a SE detector (Hitachi HD2700C) at an accelerating voltage of 200 kV. SE images exhibit 3D structure of carbon support (Figure 1b), particularly surface pores (Figure 1c). Certain Pt particles in the HAADF-STEM image (outlined with dotted lines in Figure 1f) are absent in the corresponding SE image (Figure 1c), suggesting these marked Pt particles are not exposed on the surface facing the SE detector. Notably, atomic resolution is also achieved in SE (Figure 1d). A set of SE and HAADF-STEM images was utilized to determine the location of Pt diesel oxidation catalysts supported by mesoporous silica SBA-15, revealing that highly dispersed Pt particles remained confined within the pores after aging in air at 800 °C for 5 hours.[43] The image pair also elucidated the distribution of PtCo nanoparticles across both the internal and external surfaces of Ketjenblack carbon or NH_2-modified Ketjenblack for oxygen reduction reaction (ORR).[44] Chen *et. al.* took advantage of the SE and STEM imaging to investigate the degradation mechanisms of high-content (40 wt. %) Pt/C catalysts in ORR cathode for heavy duty fuel cells.[45] Pt catalysts were supported on three different carbon-based supports, such as carbon derived from Mn-doped zeolitic imidazolate frameworks (Mn-N-C), highly graphitized porous graphitic carbon (PGC), and commercial TKK high-surface-area carbon. Figure 2 shows a set of SE and medium-angle annular dark field (MAADF)-STEM images acquired at the beginning of life and after accelerated stress test (AST, cycling potentials from 0.6

to 0.95 V vs RHE for 25,000 cycles). The Pt nanoparticles remain well-dispersed and stable in size on Mn-N-C and PGC supports, whereas significant agglomeration and detachment from the surface are observed on the commercial TKK support after the AST, highlighting the critical role of support materials in mitigating catalyst degradation during operation. Figures 2(m)-(o) show the polarization curves before and after the durability test, which involved 25,000 cycles between 0.6 to 0.95 V vs. RHE. Both the Pt/Mn-N-C and Pt/PGC catalysts exhibited minimal kinetic activity loss, with $\Delta E_{1/2}$ less than 20 mV, while the commercial Pt/TKK catalysts showed a 49 mV loss. The electrochemical surface area (ECSA) of all three catalysts was also compared before and after the durability test, revealing a significantly higher loss in ECSAs for the TKK catalyst. This demonstrates the inferior durability of the commercial catalyst, consistent with the electron microscopy observations. Identical location SE and HAADF-STEM measurements, where the same specific region of a specimen is imaged before and after the reaction, was utilized to assess changes in Pt and PtCo catalysts for ORR, in which liquid electrolyte was used during different stages of electrochemical cycling.[46]

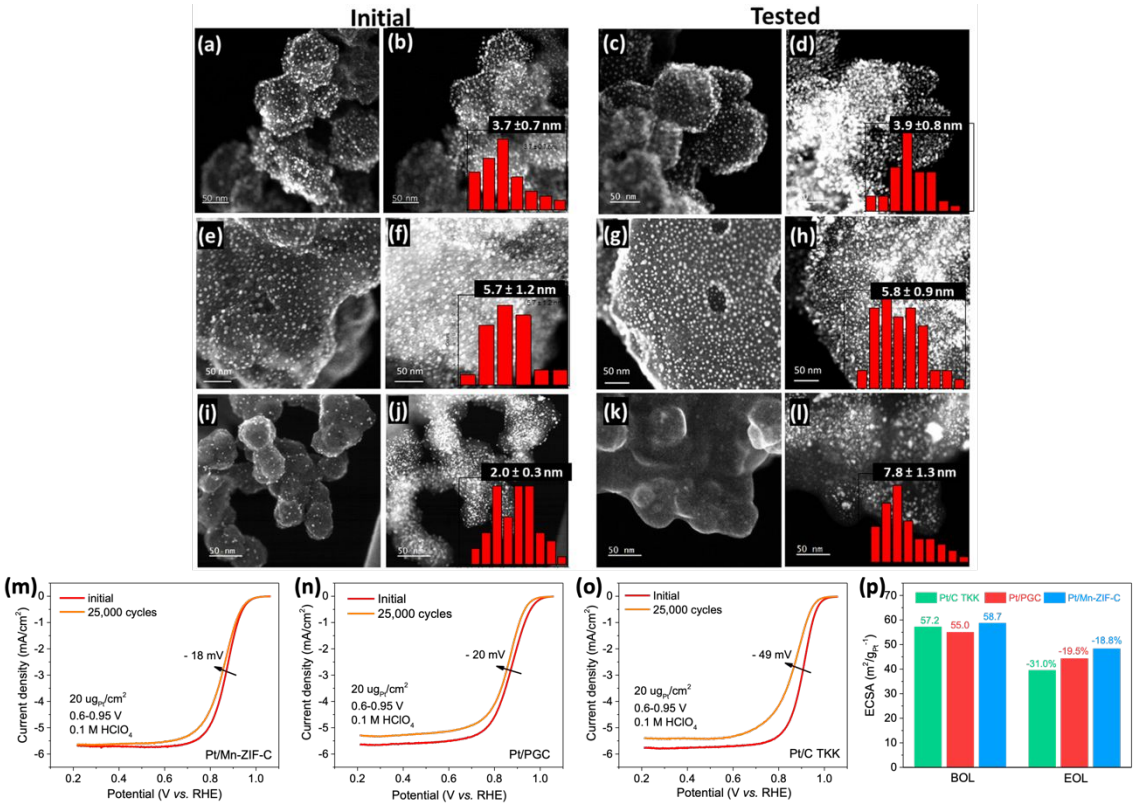

Figure 2. Two electron microscopy techniques, SE (a), (c), (e), (g), (i), and (k) and ADF-STEM (b), (d), (f), (h), (j), and (l) images, were used to analyze the morphology and nanostructure changes of three studied Pt (40. Wt%) catalysts before and after stability

AST. (a)–(d) the Pt (40. Wt%)/Mn–N–C catalyst before (a), (b) and after (c), (d) the AST. (e)–(h) the Pt (40 wt%)/PGC catalyst before (e), (f) and after (g), (h) the AST. (i)–(l) the TKK (40 wt% Pt/C) before (i), (j) and after (k), (l) the AST. The inserts are the size distribution of Pt NPs for each Pt/C catalyst before and after the stability AST. (m)–(o) Polarization curves before and after potential cycling tests for the corresponding Pt/Mn–N–C, Pt/PGC, and Pt/C TKK. (p) Electrochemical surface area of three catalysts before and after durability test.[45] Reproduced with permission. Copyright 2022, IOP Publishing, Ltd.

STEM images are generally acquired using a HAADF detector, which generates images with strong *Z*-contrast.[47] (intensity ~ Z^2, *Z*: atomic number) If the catalyst consists of metals with relatively low atomic numbers and the support contains elements with higher *Z*, or if both the metal and support have similar atomic numbers, distinguishing the metal phase using HAADF-STEM becomes less straightforward. For example, in the case of palladium (Z_{Pd}: 46) catalysts supported on ceria (Z_{Ce}: 58), complementary spectroscopy techniques are necessary to confirm the presence of Pd-based species along with HAADF-STEM or TEM images.[48-50] In contrast, SE imaging offers a clear presentation of the catalyst's surface topography, providing structural information that complements the *Z*-contrast of HAADF-STEM. Figure 3a and b show SE images of Pd-based catalysts used in the methane-to-methanol conversion reaction, supported on CeO_2 with interfacial carbon layer.[51] The presence of metallic nanoparticles on the surface of support is distinctly observed, and elemental maps (Figure 3c-f) acquired from electron energy loss spectroscopy (EELS) confirms that the nanoparticles consist of Pd, while the support material is composed of Ce. It is noteworthy that SE imaging is also compatible with spectroscopy techniques, such as EELS and energy dispersive X-ray spectroscopy (EDS).

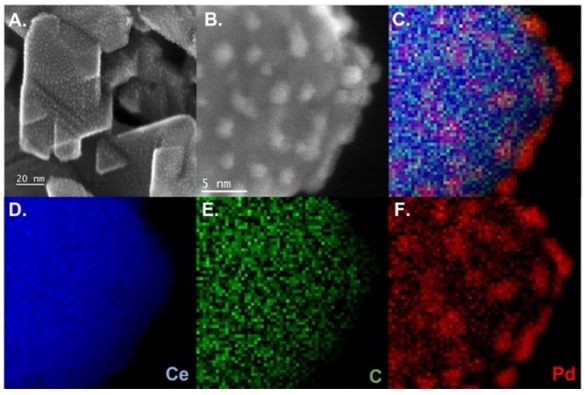

Figure 3. (A, B) SE-STEM imaging of the Pd-interfacial carbon layer on CeO_2 catalyst for the methane-to-methanol conversion reaction. (C) A combined elemental map generated using STEM-EELS, alongside individual elemental maps for Ce, C, and Pd in (D-F), respectively, obtained from the region highlighted in (B),[51] licensed under CC-BY 4.0.

In situ SE imaging

Postmortem analysis, conducted after catalyst synthesis or catalytic reactions, may present challenges in elucidating the material changes that occur during the reactions of interest. S/TEM fortunately provides insights not only into the static structural and compositional states but also into the dynamic evolution of materials under external stimuli, such as temperature variations (heating/cooling), electrical biasing, or *in situ* conditions within controlled environments (e.g., gas phases).[52, 53] In the case of catalysts under gaseous conditions, SE imaging can be a powerful technique for tracking the three dimensional evolution of catalysts *in situ* on environmental S/TEM (E-S/TEM). E-S/TEM enables the introduction of a gas environment around the specimen while maintaining vacuum integrity in the gun area through an additional differential pumping system. Using specimen holders equipped with heating capabilities allows for increasing temperature of the specimen, thereby facilitating the simulation of specific reaction conditions. The following are exemplary studies of *in situ* environmental SE imaging, which elucidates the structural changes of the catalysts under gaseous conditions to correlate these changes with their performance.

Environmental SE/STEM imaging has provided insights into the activation process of Ni-based catalyst on γ-Mo_2N for CO_2 hydrogenation.[54] A series of SE images, acquired in the flow of H_2/N_2 at a ratio of 3:1 and elevated temperatures (400 °C and 520 °C), revealed that the pre-synthesized 4 nm Ni particles undergoes reverse sintering, forming under-coordinated Ni clusters due to a strong interaction with γ-Mo_2N. This reverse sintering phenomena enhances chemoselective hydrogenation of CO_2 to CO, improving catalytic performance.

The structural evolution of Pt nanoparticles supported on carbon was systematically investigated under controlled gaseous environments (O_2, H_2O, and H_2 at ~10^{-2} Pa) and varying temperatures to elucidate catalyst deactivation mechanisms.[55] *In situ* environmental SE imaging revealed that Pt nanoparticles exhibited both lateral mobility across the carbon support and penetration through it, with these dynamics being most pronounced under oxygen exposure. *In situ* SE imaging further demonstrated degradation of the carbon support, characterized by trench formation in O_2 and H_2, likely due to erosion processes. This study revealed that multiple interrelated processes contribute to the observed transformations in supported catalysts when exposed to stimuli, including temperature fluctuations and variations in the gas-phase environment.

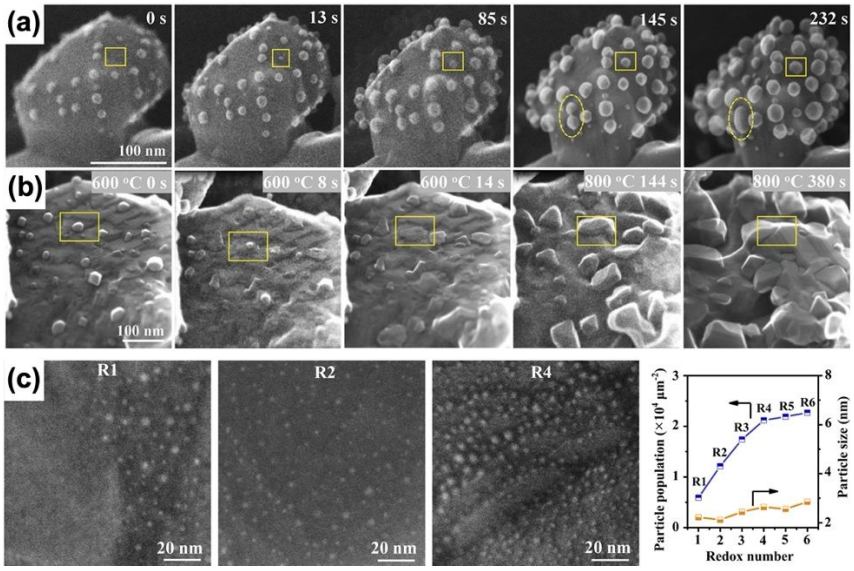

Figure 4.(a) SE images of a typical area of Co-doped $Sr_2Fe_{1.5}Mo_{0.5}O_{6-\delta}$ (SFMC) in 10 Pa of H_2 supplied at 800 °C and (b) SE mages of a SFMC area with 10 Pa of O_2 supplied at 600 °C for 22 s, then increasing from 600 to 800 °C with a heating rate of 5 °C s^{-1} and then stay at 800 °C. Time begins after supplying O_2 toward the sample.[56] Reproduced with permission. Copyright 2020, John Wiley and Sons. (c) Ex situ SE images of $Sr_2Fe_{1.4}Ru_{0.1}Mo_{0.5}O_{6-\delta}$ (SFRuM) after 1st, 2nd and 4th reduction. Population and size distribution of metal nanoparticles exsolved after different redox manipulations,[57]licensed under CC-BY 4.0.

Solid oxide electrolysis cells (SOECs) for CO_2electrolysis offer an effective means of converting renewable electrical energy into chemical energy, stored in the form of CO.[58] To improve the efficacy of CO_2 electrolysis, a novel catalyst design has been proposed, involving the dispersion of abundant metallic nanoparticles on the surface of perovskite materials.[59, 60] Understanding the formation mechanisms of these metal nanoparticles during redox reactions on the perovskite surface is essential for optimizing catalytic activity and enhancing reversibility, thereby enabling the design of highly efficient and regenerative metal-oxide interfaces for CO_2 electrolysis. SE imaging conducted under reducing and oxidizing conditions has revealed structural evolutions associated with the reversible exsolution and dissolution of metal particles within the perovskite matrix. Lv *et al.*[56] observed the emergence of CoFe alloy nanoparticles in a Co-doped $Sr_2Fe_{1.5}Mo_{0.5}O_{6-\delta}$ (SFMC) under a reducing environment of 10 Pa of H_2 at 800 °C, accompanied by a phase transformation from a double perovskite to layered perovskite (Figure 4a). Under an oxidizing condition with 10 Pa of O_2 (Figure 4b), these CoFe alloy nanoparticles were initially converted into flaky, irregular shaped $CoFeO_x$ particles that adhered to the SFMC surface at 600 °C. Upon further heating to 800 °C, the $CoFeO_x$ particles fully reverted to the perovskite phase, completing a phase transition that ultimately restores the original double perovskite structure. SFMC decorated with CoFe alloy nanoparticles exhibited enhanced CO_2 electrolysis performance

and stability than SFMC itself. Notably, their electrochemical performance was recoverable over 12 redox cycles, demonstrating the regenerative capability of the CoFe alloy nanoparticles. The same group also developed a strategy to promote exsolution of RuFe alloy nanoparticles on $Sr_2Fe_{1.4}Ru_{0.1}Mo_{0.5}O_{6-\delta}$ (SFRuM) perovskite, providing abundant metal/oxide active interfaces for CO_2 electrolysis.[57] *In situ* environmental SE imaging combined with chemical analyses using EDS and EELS revealed atomic-scale dynamics of RuFe alloy nanoparticle exsolution and dissolution on SFRuM surface. Repeated redox cycles at 600−850 °C under 10 Pa H_2 or O_2 induced Ru enrichment on the SFRuM surface, promoting the exsolution of RuFe alloy nanoparticles. Following four redox cycles, the nanoparticle density increased by approximately 3.6-fold compared to the initial reduction treatment (Figure 4c), while the nanoparticle size remained unchanged. Subsequent CO_2 electrolysis performance tests revealed that the current density progressively improved with each reduction cycle, culminating after four redox manipulations, thereby highlighting a clear structure-activity relationship.

Current Challenges and Future Outlook

Although most modern TEM provides the STEM mode and there are dedicated STEM instruments available, not all of them are equipped with the SE detector. Consequently, SE imaging in STEM may not be widely accessible. However, it is commercially available and undergoing development. Japanese microscope manufacturers, such as JEOL and Hitachi, provide SE detectors as an optional feature for their S/TEM systems.[36, 41] Hitachi has developed instrumentation for *in situ* SE and ADF-STEM imaging in gaseous environments.[61-63] Bruker, formerly known as Nion, reported development of SE detector and atomic resolution SE imaging within a 30-200 keV aberration-corrected, monochromated, ultra-high-vacuum (UHV) STEM.[64] The advantages of this system for SE imaging include higher scattering cross-sections of SE at a typical SEM operating voltage of 30 keV, reduced knock-on radiation damage, and the clean UHV environment (10^{-9} torr), all contributing to optimized conditions for high-resolution, surface-sensitive imaging. Bruker also introduced advanced instrumentation developments, including dual SE detectors positioned both below and above the specimen to enable simultaneous imaging of both surface layers (Figure 5), as well as the integration of laser optics, which allows for surface cleaning through localized heating.[65, 66]

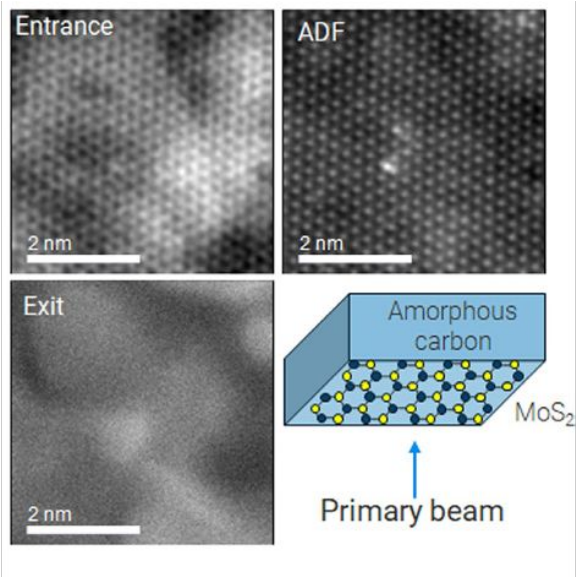

Figure 5. SE images from dual SE detectors above and below the specimen. MoS_2 monolayer on a carbon film visible in the entrance but not exist SE signal, demonstrating the ability to image Å-scale features on the surface of a bulk sample. (Results from Bruker, formerly Nion).[67]

Real time observation of catalysis requires specific reaction conditions, such as high temperatures or certain environment. For instance, SE images shown in Figure 4 were acquired at 600 and 800 °C under 10 Pa of oxygen gas. While the temperature dependency of SE emission has been reported, those studies were conducted within a limited temperature range (up to 500 K in simulation).[68, 69] The effect of temperature on SE emission and consequently, SE imaging has not been fully explored across broader temperature range relevant to catalysis. To accurately analyze images under different conditions, quantification of SE signals at varying temperatures will be necessary. To achieve a higher gas pressure around the specimen than that used in ETEM or a liquid environment, a closed cell system with hermetically sealed silicon nitride viewing windows at both the top and bottom has been employed for *in situ* S/TEM studies.[52] The presence of the top window unfortunately obstructs the detection of SE signals emitted from the specimen, imposing a fundamental limitation for SE imaging. A specialized specimen holder design, allowing SEs to escape from the specimen while maintaining the integrity of the surrounding environment, would be essential for *in situ* SE studies within closed cell systems. One possibility is to modify the top window by creating micron-sized holes to enable the escape of SEs and conduct experiments using environmental STEM. This approach would provide additional differential pumping to maintain vacuum integrity despite the gas flow from the holes in the window.

SE imaging in STEM is still an emerging field with substantial potential for further development. While atomic-resolution SE imaging has been demonstrated (Figure 1d), its application has so far been primarily limited to visualizing the morphology of catalysts. There remains significant untapped potential to leverage the unprecedented spatial resolution of SE imaging for broader applications. One key aspect involves bridging the gap between surface science and electron microscopy, facilitating the acquisition of more comprehensive, multimodal information on the specimen in its operational state. While scanning tunneling microscopy (STM), which is surface sensitive imaging technique, has offered valuable insights into catalytic reaction mechanisms at the atomic scale,[70, 71] its reliance on atomically flat surfaces can limit its applicability to the more complex, heterogeneous surfaces typical of real-world catalysts. In contrast, SE imaging in aberration-corrected STEM provides detailed surface structural information at the atomic level,[40] while conventional STEM imaging offers an overall view of the specimen. Additionally, STEM enables elemental and chemical analysis through spectroscopic techniques such as EELS an EDS, offering atomic-level insights into structure, composition, and chemical bonding.[26, 72, 73]

The rapid advancements in computational science, particularly in artificial intelligence, deep learning, and machine learning, have the potential to significantly enhance image-based information retrieval and improve the efficiency of data acquisition. Although SE images provide topographic information, 3D surface reconstruction algorithms for SEM images have proposed to generate more informative and qualitative 3D visualizations,[71, 74] which SE images acquired from STEM could also benefit from. In addition, a deep learning-assisted method has been developed for the automated analysis of large STEM image datasets.[75, 76] Pt/Co alloy nanoparticles supported on a porous substrate were efficiently quantified both in their pristine state and following fuel cell cycling.[77] SE images, whether acquired independently or simultaneously with STEM images, can leverage advanced quantitative analysis techniques for both ex situ and in situ data collection. This approach facilitates the comprehensive examination of various aspects of the specimen under diverse conditions, allowing for statistical quantification that enhances the correlation with real catalytic processes.

Acknowledgement

This research used Electron Microscopy Facilities the Center for Functional Nanomaterials (CFN), which is a U.S. Department of Energy Office of Science User Facility, at Brookhaven National Laboratory under

Contract No. DE-SC0012704. We appreciate Dr. Yimei Zhu for valuable discussions and prof. Gang Wu at Washington University in St. Louis for a Pt/C sample for figure 1.

References

1. American Chemical Society., American Institute of Chemical Engineers., Chemical Manufacturers Association (U.S.), Council for Chemical Research (U.S.) and Synthetic Organic Chemical Manufacturers Association., *Technology vision 2020 : The U.S. chemical industry*, Dept. of Government Relations and Science Policy : American Chemical Society, Washington, DC, 1996.
2. X. J. Cui, W. Li, P. Ryabchuk, K. Junge and M. Beller, *Nature Catalysis*, 2018, **1**, 385-397.
3. A. Kumar, P. Daw and D. Milstein, *Chem Rev*, 2022, **122**, 385-441.
4. C. Descorme, P. Gallezot, C. Geantet and C. George, *Chemcatchem*, 2012, **4**, 1897-1906.
5. J. M. Thomas, *Chemsuschem*, 2014, **7**, 1801-1832.
6. J. Heveling, *J Chem Educ*, 2012, **89**, 1530-1536.
7. X. Jiang, X. W. Nie, X. W. Guo, C. S. Song and J. G. G. Chen, *Chem Rev*, 2020, **120**, 7984-8034.
8. A. Dokania, A. Ramirez, A. Bavykina and J. Gascon, *ACS Energy Letters*, 2019, **4**, 167-176.
9. Z. Xu, F. S. Xiao, S. K. Purnell, O. Alexeev, S. Kawi, S. E. Deutsch and B. C. Gates, *Nature*, 1994, **372**, 346-348.
10. A. A. Herzing, C. J. Kiely, A. F. Carley, P. Landon and G. J. Hutchings, *Science*, 2008, **321**, 1331-1335.
11. M. Turner, V. B. Golovko, O. P. H. Vaughan, P. Abdulkin, A. Berenguer-Murcia, M. S. Tikhov, B. F. G. Johnson and R. M. Lambert, *Nature*, 2008, **454**, 981-U931.
12. Y. Lei, F. Mehmood, S. Lee, J. Greeley, B. Lee, S. Seifert, R. E. Winans, J. W. Elam, R. J. Meyer, P. C. Redfern, D. Teschner, R. Schlögl, M. J. Pellin, L. A. Curtiss and S. Vajda, *Science*, 2010, **328**, 224-228.
13. A. K. Galwey, P. Gray, J. F. Griffiths and S. M. Hasko, *Nature*, 1985, **313**, 668-671.
14. M. Flytzani-Stephanopoulos, S. Wong and L. D. Schmidt, *Journal of Catalysis*, 1977, **49**, 51-82.
15. R. Aiello, J. E. Fiscus, H. C. zur Loye and M. D. Amiridis, *Appl Catal a-Gen*, 2000, **192**, 227-234.
16. G. C. Grunewald and R. S. Drago, *Journal of the American Chemical Society*, 1991, **113**, 1636-1639.
17. H. J. Kwon, D. S. Yang, M. S. Koo, S. M. Ji, J. Jeong, S. Oh, S. K. Kuk, H. S. Heo, D. J. Ham, M. Kim, H. Choi, J. M. Lee, J. W. Shur, W. J. Lee, C. O. Bin, N. Timofeev, H. Q. Wu, L. M. Wang, T. W. Lee, D. J. Jacob and H. C. Lee, *Nat Commun*, 2023, **14**, 520.
18. D. A. Jefferson, J. M. Thomas, G. R. Millward, K. Tsuno, A. Harriman and R. D. Brydson, *Nature*, 1986, **323**, 428-431.
19. M. M. J. Treacy, A. Howie and C. J. Wilson, *Philos Mag A*, 1978, **38**, 569-585.
20. S. J. Pennycook, *J Microsc.*, 1981, **124**, 15-22.
21. M. H. Yao, D. J. Smith and A. K. Datye, *Ultramicroscopy*, 1993, **52**, 282-288.
22. P. D. Nellist and S. J. Pennycook, *Science*, 1996, **274**, 413-415.
23. Z. Y. Li, N. P. Young, M. Di Vece, S. Palomba, R. E. Palmer, A. L. Bleloch, B. C. Curley, R. L. Johnston, J. Jiang and J. Yuan, *Nature*, 2008, **451**, 46-48.
24. P. E. Batson, N. Dellby and O. L. Krivanek, *Nature*, 2002, **418**, 617-620.
25. J. Z. Li, M. J. Chen, D. A. Cullen, S. Hwang, M. Y. Wang, B. Y. Li, K. X. Liu, S. Karakalos, M. Lucero, H. G. Zhang, C. Lei, H. Xu, G. E. Sterbinsky, Z. X. Feng, D. Su, K. L. More, G. F. Wang, Z. B. Wang and G. Wu, *Nature Catalysis*, 2018, **1**, 935-945.
26. H. T. Chung, D. A. Cullen, D. Higgins, B. T. Sneed, E. F. Holby, K. L. More and P. Zelenay, *Science*, 2017, **357**, 479-483.

27. M. Weyland and P. A. Midgley, *Materials Today*, 2004, **7**, 32-40.
28. W. Albrecht and S. Bals, *J Phys Chem C*, 2020, **124**, 27276-27286.
29. D. B. Williams and C. B. Carter, *Transmission Electron Microscopy : A Textbook for Materials Science*, Springer US : Imprint: Springer,, New York, NY, 1st edn., 1996.
30. H. Seiler, *J Appl Phys*, 1983, **54**, R1-R18.
31. L. Reimer, *Scanning electron microscopy : physics of image formation and microanalysis*, Springer, Berlin ; New York, 2nd edn., 1998.
32. D. Imeson, R. H. Milne, S. D. Berger and D. Mcmullan, *Ultramicroscopy*, 1985, **17**, 243-249.
33. D. Imeson, *J Microsc.*, 1987, **147**, 65-74.
34. A. L. Bleloch, A. Howie and R. H. Milne, *Ultramicroscopy*, 1989, **31**, 99-110.
35. J. Liu and J. M. Cowley, *Ultramicroscopy*, 1991, **37**, 50-71.
36. Y. Zhu, H. Inada, K. Nakamura and J. Wall, *Nat Mater*, 2009, **8**, 808-812.
37. H. Inada, D. Su, R. F. Egerton, M. Konno, L. Wu, J. Ciston, J. Wall and Y. Zhu, *Ultramicroscopy*, 2011, **111**, 865-876.
38. L. J. Wu, R. F. Egerton and Y. M. Zhu, *Ultramicroscopy*, 2012, **123**, 66-73.
39. H. G. Brown, A. J. D'Alfonso and L. J. Allen, *Phys Rev B*, 2013, **87**, 054102.
40. J. Ciston, H. G. Brown, A. J. D'Alfonso, P. Koirala, C. Ophus, Y. Lin, Y. Suzuki, H. Inada, Y. Zhu, L. J. Allen and L. D. Marks, *Nat Commun*, 2015, **6**, 7358.
41. D. R. G. Mitchell and G. Casillas, *Microscopy Today*, 2016, **24**, 22-27.
42. S. Hwang, L. J. Wu, K. Kisslinger, J. Yang, R. Egerton and Y. Zhu, *Ultramicroscopy*, 2024, **261**, 113967.
43. H. N. Pham, J. Y. Howe, A. Ghosh, M. Melton, D. Kunwar, E. J. Peterson and A. K. Datye, *Microsc Microanal*, 2018, **24 (S1)**, 1700-1701.
44. Q. Gong, H. Zhang, H. R. Yu, S. Jeon, Y. Ren, Z. Z. Yang, C. J. Sun, E. A. Stach, A. C. Foucher, Y. K. Yu, M. Smart, G. M. Filippelli, D. A. Cullen, P. Liu and J. Xie, *Matter*, 2023, **6**, 963-982.
45. M. J. Chen, C. Z. Li, B. Z. Zhang, Y. C. Zeng, S. Karakalos, S. Hwang, J. Xie and G. Wu, *Journal of the Electrochemical Society*, 2022, **169**, 034510.
46. H. Yu, M. J. Zachman, C. Li, L. Hu, N. N. Kariuki, R. Mukundan, J. Xie, K. C. Neyerlin, D. J. Myers and D. A. Cullen, *ACS Applied Materials & Interfaces*, 2022, **14**, 20418-20429.
47. O. L. Krivanek, M. F. Chisholm, V. Nicolosi, T. J. Pennycook, G. J. Corbin, N. Dellby, M. F. Murfitt, C. S. Own, Z. S. Szilagyi, M. P. Oxley, S. T. Pantelides and S. J. Pennycook, *Nature*, 2010, **464**, 571-574.
48. E. M. Slavinskaya, R. V. Gulyaev, A. V. Zadesenets, O. A. Stonkus, V. I. Zaikovskii, Y. V. Shubin, S. V. Korenev and A. I. Boronin, *Applied Catalysis B-Environmental*, 2015, **166**, 91-103.
49. V. Muravev, A. Parastaev, Y. van den Bosch, B. Ligt, N. Claes, S. Bals, N. Kosinov and E. J. M. Hensen, *Science*, 2023, **380**, 1174-1178.
50. D. Gashnikova, F. Maurer, E. Sauter, S. Bernart, J. Jelic, P. Dolcet, C. B. Maliakkal, Y. M. Wang, C. Wöll, F. Studt, C. Kübel, M. Casapu and J. D. Grunwaldt, *Angewandte Chemie-International Edition*, 2024, **63**, e202408511.
51. J. D. Jiménez, P. G. Lustemberg, M. Danielis, E. Fernández-Villanueva, S. Hwang, I. Waluyo, A. Hunt, D. Wierzbicki, J. Zhang, L. Qi, A. Trovarelli, J. A. Rodriguez, S. Colussi, M. V. Ganduglia-Pirovano and S. D. Senanayake, *Journal of the American Chemical Society*, 2024, **146**, 25986-25999.
52. S. Hwang, X. B. Chen, G. W. Zhou and D. Su, *Advanced Energy Materials*, 2020, **10**, 1902105.
53. H. Y. Chao, K. Venkatraman, S. Moniri, Y. J. Jiang, X. Tang, S. Dai, W. P. Gao, J. W. Miao and M. F. Chi, *Chem Rev*, 2023, **123**, 8347-8394.
54. L. L. Lin, J. J. Liu, X. Liu, Z. R. Gao, N. Rui, S. Y. Yao, F. Zhang, M. L. Wang, C. Liu, L. L. Han, F. Yang, S. Zhang, X. D. Wen, S. D. Senanayake, Y. C. Wu, X. N. Li, J. A. Rodriguez and D. Ma, *Nat Commun*, 2021, **12**, 6978.
55. S. Lee, K. Gadelrab, L. Cheng, J. P. Braaten, H. L. Wu and F. M. Ross, *ACS Nano*, 2024, **18**, 21258-21267.

56. H. Lv, L. Lin, X. Zhang, Y. Song, H. Matsumoto, C. Zeng, N. Ta, W. Liu, D. Gao, G. Wang and X. Bao, *Advanced Materials*, 2020, **32**, 1906193.
57. H. Lv, L. Lin, X. Zhang, R. Li, Y. Song, H. Matsumoto, N. Ta, C. Zeng, Q. Fu, G. Wang and X. Bao, *Nat Commun*, 2021, **12**, 5665.
58. Y. F. Song, X. M. Zhang, K. Xie, G. X. Wang and X. H. Bao, *Advanced Materials*, 2019, **31**, 1902033.
59. J. H. Myung, D. Neagu, D. N. Miller and J. T. S. Irvine, *Nature*, 2016, **537**, 528-531.
60. J. H. Kim, J. K. Kim, J. Liu, A. Curcio, J. S. Jang, I. D. Kim, F. Ciucci and W. Jung, *ACS Nano*, 2021, **15**, 81-110.
61. H. Matsumoto, T. Sato, K. Nakano, T. Yaguchi, I. Nagaoki and Y. Nagakubo, *Microsc Microanal*, 2013, **19**, 464.
62. H. Matsumoto, T. Sato, K. Igarashi, T. Hashimoto and H. Inada, *Microsc Microanal*, 2023, **29**, 122-123.
63. H. Inada, H. Kikuchi, A. Hanawa, Y. Suzuki, M. Shirai and K. Nakamura, *Microsc Microanal*, 2018, **24**, 318-319.
64. M. T. Hotz, J. Martis, T. Radlicka, N. J. Bacon, N. Dellby, T. C. Lovejoy, S. C. Quillin, H. Y. Hwang, P. Singh and O. L. Krivanek, *Microsc Microanal*, 2023, **29**, 2064-2065.
65. B. Plotkin-Swing, J. Martis, C. Su, M. T. Hotz, N. Dellby, T. Radlicka, O. L. Krivanek and T. C. Lovejoy, *Microsc Microanal*, 2024, **30**, 1480-1482.
66. J. Martis, B. Plotkin-Swing, B. Haas, T. Susi, M. T. Hotz, O. L. Krivanek, N. Dellby, A. Mittelberger, S. C. Quillin and T. C. Lovejoy, *Microsc Microanal*, 2024, **30**, 2182-2184.
67. Bruker, Atomic Resolution Imaging with Secondary Electrons Flyer, https://www.bruker.com/en/products-and-solutions/microscopes/electron-microscopes.html, (accessed Feb. 27, 2025).
68. P. Zhang, *Appl Phys a-Mater*, 2024, **130**, 37.
69. M. I. Khan, S. D. Lubner, D. F. Ogletree and C. Dames, *J Appl Phys*, 2018, **124**, 195104.
70. G. Kyriakou, M. B. Boucher, A. D. Jewell, E. A. Lewis, T. J. Lawton, A. E. Baber, H. L. Tierney, M. Flytzani-Stephanopoulos and E. C. H. Sykes, *Science*, 2012, **335**, 1209-1212.
71. L. Xu, K. G. Papanikolaou, B. A. J. Lechner, L. Je, G. A. Somorjai, M. Salmeron and M. Mavrikakis, *Science*, 2023, **380**, 70-76.
72. Y. Li, N. M. Adli, W. T. Shan, M. Y. Wang, M. J. Zachman, S. Hwang, H. Tabassum, S. Karakalos, Z. X. Feng, G. F. Wang, Y. C. Li and G. Wu, *Energy & Environmental Science*, 2022, **15**, 2108-2119.
73. Y. C. Zeng, J. S. Liang, C. Z. Li, Z. Qiao, B. Y. Li, S. Hwang, N. N. Kariuki, C. W. Chang, M. Y. Wang, M. Lyons, S. Lee, Z. X. Feng, G. F. Wang, J. Xie, D. A. Cullen, D. J. Myers and G. Wu, *Journal of the American Chemical Society*, 2023, **145**, 17643-17655.
74. A. P. Tafti, J. D. Holz, A. Baghaie, H. A. Owen, M. M. He and Z. Y. Yu, *Micron*, 2016, **87**, 33-45.
75. G. Roberts, S. Y. Haile, R. Sainju, D. J. Edwards, B. Hutchinson and Y. Y. Zhu, *Sci Rep-Uk*, 2019, **9**.
76. K. Lee, J. Park, S. Choi, Y. Lee, S. Lee, J. Jung, J. Y. Lee, F. Ullah, Z. Tahir, Y. S. Kim, G. H. Lee and K. Kim, *Nano Letters*, 2022, **22**, 4677-4685.
77. S. H. Yang, E. B. Park, S. Y. Cho, Y. S. Kang, H. A. Ju, Y. Jeon, D. Yang, S. D. Yim, S. Lee and Y. M. Kim, *Mater Today Energy*, 2023, **36**, 101348.

Data Availability Statement

All data presented in this study are included in the main text (Figure 1). Additional data used to generate figures have been reproduced with permission from previously published sources.